ADVANCED FUNCTIONAL MATERIALS
www.afm-journal.de

Integrated Dual-Phase Ion Transport Design Within Electrode for Fast-Charging Lithium-Ion Batteries

*Shuibin Tu, Yan Zhang, Dongsheng Ren, Zihe Chen, Wenyu Wang, Renming Zhan, Xiancheng Wang, Kai Cheng, Yangtao Ou, Xiangrui Duan, Li Wang, and Yongming Sun**

The development of fast-charging lithium-ion batteries with high energy density is hindered by the sluggish Li^+ transport and substantial polarization within graphite electrodes. Herein, this study proposes that the integrated design of liquid electrolyte and solid electrolyte, a dual-phase electrolyte (DP-electrolyte), can facilitate Li^+ transport within a thick electrode. A 3D Li_3PS_4 (LPS) network is constructed within the graphite electrode to form the LPS/graphite electrode. This is achieved through the in situ conversion of the P_4S_{16} into the LPS, a process introduced during the slurry processing. Both experimental findings and simulation outcomes indicate that this design mitigates the concentration polarization due to the improved Li^+ transport capability with an overall high Li^+ transference number within the electrode. With a high capacity of ≈3.1 mAh cm^{-2} attributed to the graphite electrode, the $LiNi_{0.6}Co_{0.2}Mn_{0.2}O_2$ (NCM622)||LPS/graphite cells demonstrate superior fast-charging capability (4 C, 15 min, charging to ≈87.7%) and stable cycling performance (4 C, 700 cycles, ≈80% capacity retention). Furthermore, they exhibit commendable low-temperature performance. The Ah-level pouch cell achieves 87.5% recharge in 15 min with an energy density of ≈221.5 Wh kg^{-1}. This work offers an alternative avenue for the advancement of fast-charging lithium-ion batteries with practical high energy density.

1. Introduction

The development of lithium-ion batteries (LIBs) that exhibit both high energy density and fast charging capabilities is urgently needed to expedite the widespread adoption of electric vehicles (EVs) and support other burgeoning applications.[1] The objective set forth by the US Department of Energy is to achieve an 80% state of charge within the 15 min timeframe, predicated on a cell-level energy density of 200 Wh kg^{-1}.[2] The state-of-the-art graphite anode is perceived as a constraining factor that impedes the fast charging capability of commercial LIBs,[3] attributable to its sluggish Li^+ transport behavior at the material/electrode interface and within the porous electrode structure. Despite the advantage of achieving high energy density in batteries, the low equilibrium potential of graphite (≈0.1 V vs Li/Li^+) can easily induce metallic Li plating on its surface during rapid charging operations.[4] This occurrence leads to swift capacity degradation of batteries and even raises safety concerns. To date, it continues to be a significant challenge to strike a balance between the energy density and fast charging capability of LIBs.

Over the past years, strategies including bulk graphite design and solid electrolyte interface (SEI) engineering have demonstrated great potential for improving Li^+ transport kinetics at the material/interface.[4c,5] Despite the advancements, these reported graphite anodes are usually constrained by electrode parameters, such as low areal capacities (e.g.,<2 mAh cm^{-2}) or high electrode porosities, which constraints significantly compromise the energy density of LIBs. Very recently, our group has effectively developed a continuous Li_3P based-SEI on the graphite anode,[5d] characterized by high ionic conductivity and low surficial Li^+ ion desolvation energy, which significantly enhances Li^+ transport at the electrode/electrolyte interface, thereby facilitating rapid charging capability of batteries (charging to ≈91.2% under 6 C, areal capacity of 2.3 mAh cm^{-2}) in Ah-level pouch cell configuration. It is imperative to adopt reasonably high areal capacities of electrodes (e.g., >3 mAh cm^{-2}) for high-energy-density LIBs, assuming other battery parameters remain unchanged. Unfortunately, the fast-charging capability of thick graphite electrodes is often constrained by the sluggish Li^+ transport behavior at the electrode level, which results in severe concentration polarization during the fast-charging process.[1b,6] Constructing electrode structures with high porosity could potentially expedite the Li^+ transport within the graphite electrodes,[6a,7] which, however, often compromises the

S. Tu, Y. Zhang, Z. Chen, W. Wang, R. Zhan, X. Wang, K. Cheng, Y. Ou, X. Duan, Y. Sun
Wuhan National Laboratory for Optoelectronics
Huazhong University of Science and Technology
Wuhan 430074, China
E-mail: yongmingsun@hust.edu.cn

S. Tu, K. Cheng
Department of Materials Science and Engineering
Huazhong University of Science and Technology
Wuhan 430074, China

D. Ren, L. Wang
Institute of Nuclear & New Energy Technology
Tsinghua University
Beijing 100084, China

The ORCID identification number(s) for the author(s) of this article can be found under https://doi.org/10.1002/adfm.202402077

DOI: 10.1002/adfm.202402077

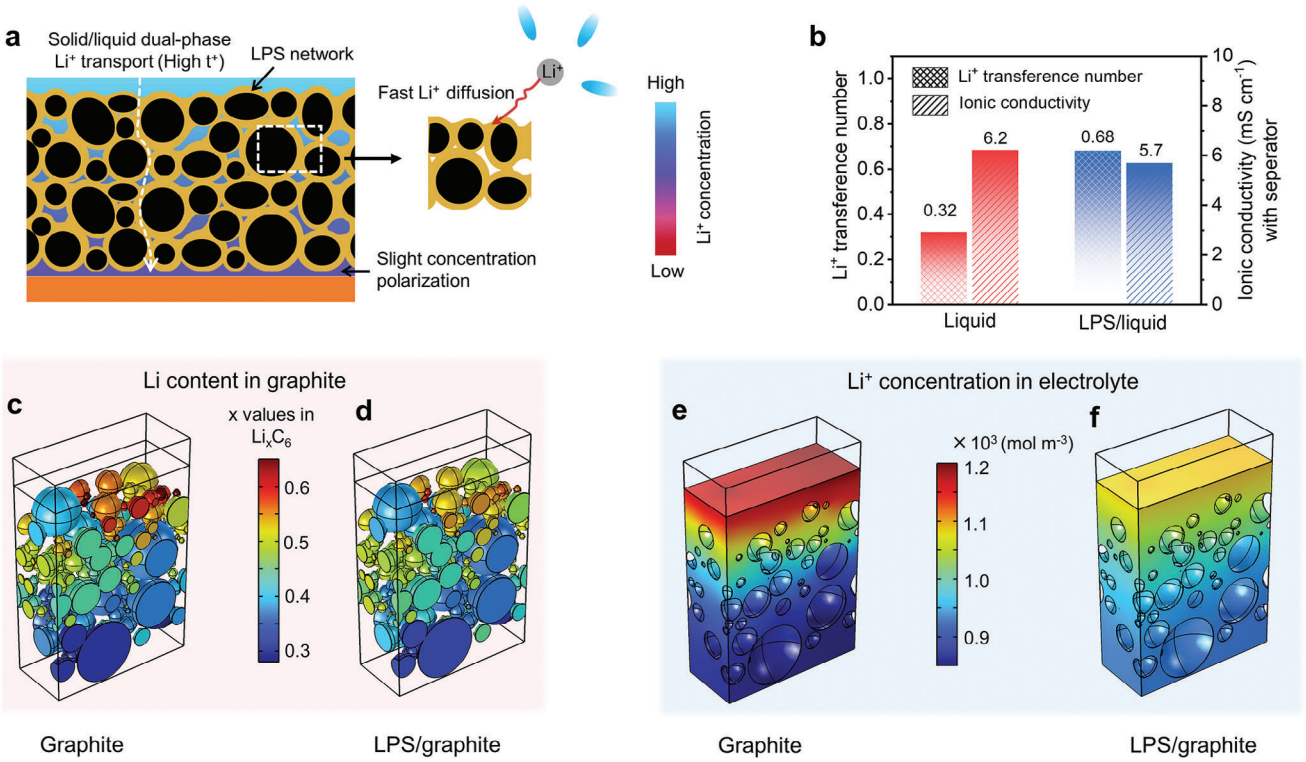

Figure 1. a) Schematic illustration of the structure and Li^+ transport within the LPS/graphite electrode. b) Ionic conductivity (with separator) and Li^+ transference number of the regular liquid electrolyte and LPS/liquid hybrid electrolyte. c–f) Simulation of Li content distribution in the graphite particle (c,d) and Li^+ concentration in electrolyte (e,f).

overall volumetric energy density of batteries due to the low tap density of electrodes. Besides, the manipulation of electrolyte chemistries, including lithium salts, solvents, and additives, has demonstrated significant potential in mitigating concentration polarization in porous electrodes by enhancing the intrinsic characteristics of Li^+ conductivity in the liquid electrolyte.[8] Nonetheless, the fast-charging performance of graphite electrodes with practical areal capacities (e.g., >3 mAh cm^{-2}) remains significantly below anticipated levels. Particularly, the subpar cycling stability under fast charging conditions poses a substantial challenge.

In this study, we propose a strategy of hybrid solid/liquid electrolyte design aimed at enhancing the apparent Li^+ transference number (t^+) in electrolyte in porous electrodes to facilitate the migration of Li^+ ions and mitigate electrode polarization under fast charging conditions. A graphite electrode with uniformly distributed P_4S_{16} was fabricated utilizing regular slurry processing operation. The Li_3PS_4 (LPS)/graphite electrode featuring an embedded 3D uniform LPS network with high ionic conductivity and t^+ value was realized via in situ lithiation of P_4S_{16} into LPS. Consequently, predicated on a commendably high anode areal capacity of ≈3.1 mAh cm^{-2}, the $LiNi_{0.6}Co_{0.2}Mn_{0.2}O_2$ (NCM622)||LPS/graphite full cells demonstrated gratifying fast-charging capability, achieving ≈87.7% of the capacity at a 4 *C* (15 min) charge rate. Furthermore, these cells maintained ≈80% capacity retention over 700 cycles under a 4 *C* charge rate, in addition to exhibiting robust low-temperature performance (−20 °C, ≈60.2% capacity retention). As a demonstration, an Ah-level NCM622||LPS/graphite pouch cell delivered an energy density of ≈221.5 Wh kg^{-1} with a charging time of 15 min. This work provides new insights for facilitating Li^+ transport in thick electrodes and presents significant potential for fast-charging LIBs with high energy density, owing to its commendable industrial compatibility.

2. Results and Discussion

In addition to the Li^+ conductivity of electrolyte, the t^+ serves as a crucial parameter for battery performance.[9] An elevated t^+ value signifies a higher proportion of migrating Li^+ within the electrolyte, indicative of a more efficient charge transfer process between the anode and cathode. An increase in t^+ is associated with a significant reduction in overpotential (polarization) during the charging process. A higher t^+ correlates with a diminished requirement for the ionic conductivity of electrolytes. For example, should the t^+ of the electrolyte attain a value of 0.8, the necessity for ionic conductivity can be mitigated by up to 50%.[10] Sulfide solid electrolytes are renowned for their high ionic conductivity and single-ion conductor characteristics with high t^+ value ($t^+ = 1$).[11] We posit that the incorporation of thiophosphate (Li_3PS_4, LPS), a typical sulfide solid electrolyte, into the graphite electrode, could enhance the overall value of t^+, in addition to the ionic conductivity, thereby substantially improving the fast charging performance (**Figure 1a**). We fabricated a graphite electrode with uniformly distributed P_4S_{16}, utilizing regular slurry processing operation. LPS/graphite electrode featuring an

embedded 3D uniform LPS network was realized via in situ lithiation of P_4S_{16} into LPS. To demonstrate the superior Li^+ transport capability afforded by the embedded LPS network, both the Li^+ conductivity and t^+ were quantified. Despite the LPS/liquid hybrid electrolyte and regular liquid electrolyte exhibiting comparable ionic conductivity values (Figure 1b; Figure S1, Supporting Information), the LPS/liquid electrolyte displayed a t^+ approximately twice that of the regular electrolyte (≈0.68 vs ≈0.32) (Figure 1b; Figure S2, Supporting Information). These results suggested that the hybrid LPS/liquid design can effectively increase the t^+ without significantly reducing the ionic conductivity. Consequently, the LPS/graphite electrode, endowed with solid/liquid dual-phase Li^+ transport capability, has the potential to mitigate Li^+ concentration gradients and enhance the Li^+ transfer at the particle/electrode levels. To probe the impact of the solid/liquid dual-phase Li^+ transport mechanism on augmenting the reaction kinetics of the graphite electrode, we simulated the distributions of the local state of charge (SOC) at the graphite particle surface and Li^+ concentration in the liquid electrolyte during fast lithiation process, utilizing COMSOL software. As depicted in Figure 1c–f, the regular graphite electrode showed obvious reaction inhomogeneities at the onset of the 4 *C* lithiation process. Lithiation initially transpired at the graphite particles located on the electrode surface adjacent to the separator, and substantial gradients were discernible in the Li^+ concentration within the liquid electrolyte, with a noticeable accumulation of Li^+ at the electrode surface (Figure 1c). The disparity between local SOCs of the graphite particle amplified as the lithiation process progressed (Figure S3a, Supporting Information), signifying pronounced inhomogeneity within the porous graphite electrode. Concurrently, the distribution of the Li^+ concentration within the liquid electrolyte remained consistent throughout the 4 *C* lithiation process (Figure 1e; Figure S3b, Supporting Information). In contrast, the LPS/graphite electrode demonstrated less heterogeneous distributions of particle-surface SOC (Figure 1d; Figure S4a, Supporting Information) and Li^+ concentration within the liquid electrolyte (Figure 1f; Figure S4b, Supporting Information) during the 4 *C* lithiation process. In comparison to the regular graphite electrode, a significantly elevated Li^+ concentration in the vicinity of the current collector was observed within the LPS/graphite electrode (Figure S4b, Supporting Information), primarily attributable to its enhanced t^+ and reduced concentration polarization. Consequently, based on the simulation results, it can be inferred that the solid/liquid dual-phase Li^+ transport mechanism within the LPS/graphite electrode optimized the Li^+ transport process, thereby augmenting the reaction inhomogeneity and fast-charging performance of batteries.

The LPS/graphite electrode was fabricated by integrating the traditional slurry coating procedure with the in situ lithiation of the P_4S_{16} precursor. Firstly, the P_4S_{16} compound was synthesized via the reaction between P_4S_{10} and elemental sulfur (S) with a molar ratio of 1:6 in 300 °C (Figure S5, Supporting Information). The Raman spectra of the as-obtained P_4S_{16} exhibited characteristic peaks corresponding to S—P (100–450 cm^{-1}), S—S (480.1 cm^{-1}) and P═S bonds (694.4 and 715.4 cm^{-1}),[12] which distinguished from the red phosphorus (P) and elemental S (Figure S6, Supporting Information). The structure of P_4S_{16} was further verified by X-ray photoelectron spectroscopy (XPS) analyses. The high-resolution S 2p XPS spectrum of the P_4S_{16} compound revealed the typical characteristics of the P═S and S—P bonds at 161.9 and 163.4 eV,[13] respectively, corroborating the formation of the S—P compound (Figure S7, Supporting Information). The P_4S_{16}/graphite electrode can be fabricated by the traditional slurry coating processing with 1-methyl-2-pyrrolidinone (NMP) serving as the solvent due to the good solubility of the P_4S_{16} in NMP (Figure S8, Supporting Information). Owning to the strong affinity properties between C and S elements,[5d] the P_4S_{16} could be uniformly distributed on the graphite surface (Figure S9, Supporting Information). The chemical/electrochemical lithiation of P_4S_{16} yields the LPS,[14] culminating in the creation of the LPS/graphite electrode with a 3D LPS network within the electrode (**Figure 2**a; Figure S10, Supporting Information). Although the integration of LPS into the graphite electrode might lead to a marginal decrease in electronic conductivity, it simultaneously bolsters the Li^+ transfer capability within the electrode, a factor that is predominantly considered as the primary limiting constraint for the fast charging of thick electrodes. Contrary to the direct fabrication and utilization of LPS, the in situ generation of LPS circumvents its exposure to ambient conditions and potential side reactions with moisture. This approach thereby guarantees superior stability and high Li^+ conductivity of LPS. The as-fabricated LPS/graphite electrode exhibited a thickness of ≈75 µm, with materials loading of ≈9.9 mg cm^{-2}, as depicted in Figure 2b. This corresponds to a tap density of ≈1.3 mg cm^{-2}, a value closely aligned with that of a commercial graphite anode. Energy dispersive spectroscopic (EDS) mapping images of the LPS/graphite electrode revealed a uniform distribution of S and P elements across the graphite surface (Figure S11, Supporting Information), as well as within the electrode pore (Figure 2c,d). Scanning transmission electron microscopy (STEM), in conjunction with the corresponding elemental mapping images, further corroborates the homogeneous distribution of P and S elements on the graphite surface of the LPS/graphite electrode (Figure 2e). The above observations substantiate the formation of a 3D Li^+ conductivity network of LPS within the graphite electrode. High-resolution transmission electron microscopy (HRTEM) image revealed a crystalline layer exhibiting a d-spacing of 0.194 nm (Figure 2f). This characteristic corresponds to the (620) crystal plane of LPS (PDF No. 76–0973), thereby providing evidence for the formation of an LPS layer on the graphite surface. The formation of LPS was further demonstrated by XPS analyses (Figure 2g,h). The high-resolution P 2p XPS spectrum of the LPS/graphite electrode could be deconvoluted into three distinct peaks, with peaks located at 132.8 and 133.4 eV, attributable to the PS_4^{3-}.[13,15] (Figure 2g). The high-resolution S 2p spectrum exhibited four peaks at 161.6, 162.8, 163.5, and 164.5 eV, which were ascribed to the PS_4^{3-}, P═S, and P—S—P bonds[16] (Figure 2h), respectively.

The Li^+ transfer kinetics of the LPS/graphite electrode were scrutinized via cyclic voltammetry measurements, employing different scan rates ranging from 0.01 to 0.2 mV s^{-1} (**Figure 3**a). Notably, the LPS/graphite electrode exhibited pronounced deintercalation peaks at lower potentials in comparison to the graphite electrode (Figure S12, Supporting Information) across various scan rates, thereby confirming its superior Li^+ transport behavior. Furthermore, a linear relationship was observed between the anodic (denoted as A_1-A_3)/cathodic (denoted as C_1-C_3) peaks current (I_p) of graphite electrodes and the corresponding square root

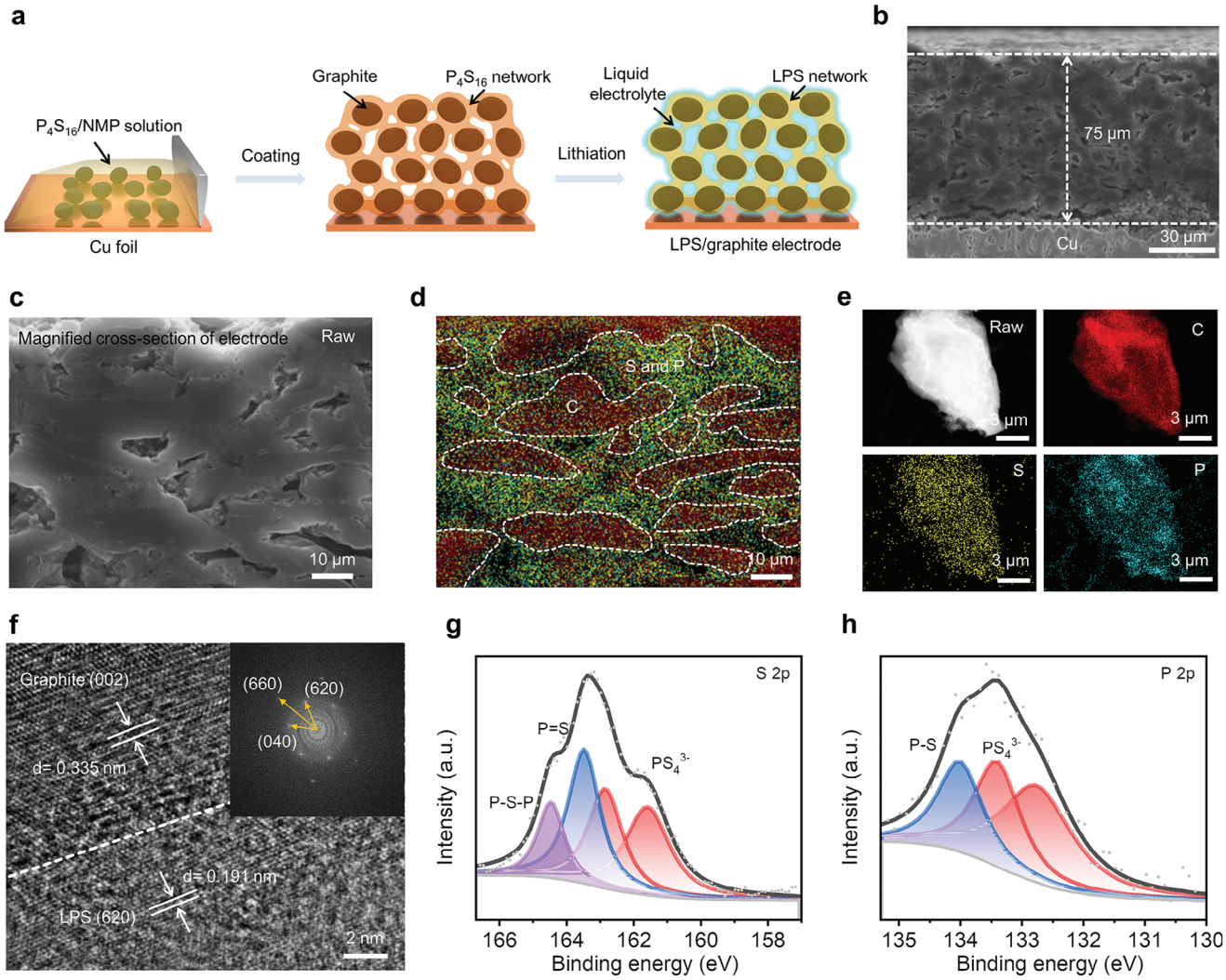

Figure 2. a) Schematic illustration of the fabrication of the LPS/graphite electrode. b) Cross-section SEM image of the LPS/graphite electrode fabricated by focused ion beam. c,d) Magnified cross-section SEM image (c) and the corresponding elemental mapping images (d) of the LPS/graphite electrode. Element color representation: red for C, yellow for S, and cyan for P. e,f) STEM and the corresponding elemental mapping (e) and HRTEM images (f) of the LPS/graphite. g,h) High-resolution P 2p (g) and S 2p (h) XPS spectra of the LPS/graphite electrode.

of the scan rate, implying a diffusion-controlled Li^+ ion transport mechanism within the electrodes (Figure 3b,c). The corresponding slope was calculated, exhibiting a direct proportionality to the Li^+ diffusion coefficient. The values of fitting slope in the LPS/graphite electrode during the Li^+ intercalation (Figure 3b) and deintercalation (Figure 3c) processes were markedly higher than those in the regular graphite electrode, thereby unveiling its accelerated Li^+ diffusion capability. The galvanostatic intermittent titration technique (GITT) was employed to scrutinize the overpotentials during the Li^+ intercalation/deintercalation processes within the graphite electrodes. The representative potential fluctuations during Li^+ intercalation and relaxation processes at open-circuit, observed in the middle profiles during GITT tests (Figure 3d,e). The total potential increase of the regular graphite electrode (≈103 mV) was much higher than that of the LPS/graphite electrode (≈53 mV). Analogous observations were also made during the Li^+ deintercalation process, with overpotentials of ≈72 and ≈105 mV for the LPS/graphite and regular graphite electrodes (Figure S13, Supporting Information), respectively. The substantial overpotential observed in the regular graphite electrode can be attributed to its elevated high interfacial resistance and significant concentration polarization within the electrode, leading to lethargic reaction kinetics. Temperature-dependent electrochemical impedance spectroscopy (EIS) was performed as function of temperature to elucidate the Li^+ transport kinetics at the electrode interface. Primarily, the SEI resistance (R_{SEI}) and charge transfer resistance (R_{ct}) values of the LPS/graphite electrode were significantly lower than those of the regular graphite electrode (Figure S14, Supporting Information). By fitting the EIS profiles to the equivalent circuit model established at different frequencies (Figure S15, Supporting Information), the activation energy of Li^+ transport across the SEI ($E_{a,SEI}$) can be ascertained using the classic Arrhenius law. A notable $E_{a,SEI}$ of ≈35.1 kJ mol^{-1} was determined for the LPS/graphite

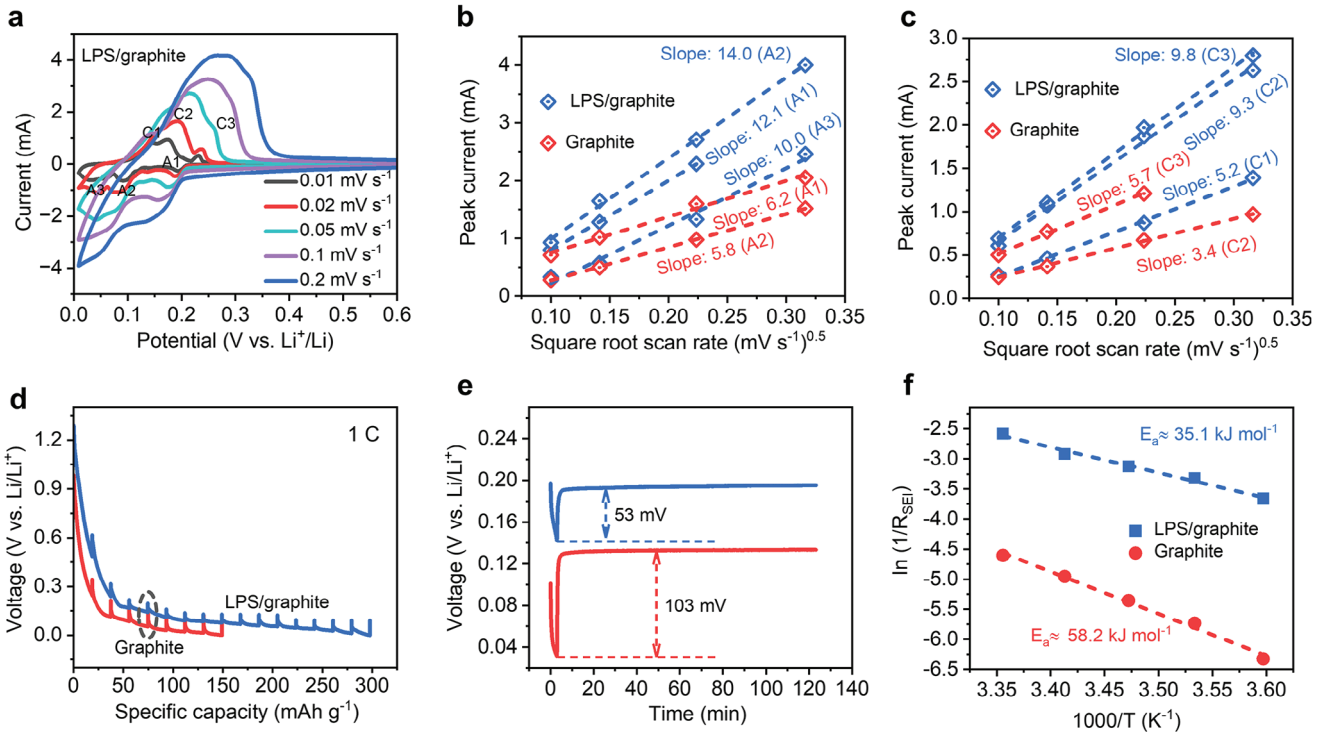

Figure 3. a) Cyclic voltammetry profiles of LPS-L/graphite electrode at various scanning rates range from 0.01 to 0.2 mV s^{-1}. b,c) Demonstration of the linear relationship between the anodic/cathodic peak current (Ip) and the square root of the scan rate ($v^{1/2}$) of two graphite electrodes. d) Discharging curves of the two graphite electrodes in half cells via GITT measurements at 1 *C*. e) The relaxation process during the rest taken from the black ellipses in Figure 3d. f) Comparison of $E_{a,SEI}$ for the two graphite electrodes. The activation energies were calculated by the classic Arrhenius law according to the EIS results.

electrode, significantly lower than that of the regular graphite electrode (≈58.2 kJ mol^{-1}) (Figure 3f), indicating the improved Li^+ transfer capability of the LPS/graphite electrode at the electrode/electrolyte interface. This can be attributed to the high ionic conductivity facilitated by the existing presence of the LPS network within the LPS/graphite electrode. These findings suggested that the LPS/graphite electrode exhibits superior reaction kinetics compared to the regular graphite electrode. This conclusion was also corroborated in the full-cell configuration (Figure S16, Supporting Information). The full cells with NCM622 cathode and LPS/graphite anode demonstrated a superior capacity retention rate and more stable cycling performance compared to those with regular graphite electrodes at various *C* rates. Typically, the capacity of the NCM622||LPS/graphite cell, recorded at 167.1 mAh g^{-1} at 4 *C*, was notably higher than that of the NCM622||graphite cell (138.8 mAh g^{-1}).

The fast-charging capabilities of the LPS/graphite electrode were meticulously evaluated in pouch cells, which were coupled with NCM622 cathodes. As shown in **Figures** 4a and S17 (Supporting Information), the cells underwent rigorous testing via a pragmatic constant current (CC)-constant voltage (CV) charging protocol. This protocol encompassed a variety of CC charging rates, spanning from 0.2 *C* to 6 *C*, where the *C* rate was determined by the charging duration, with 1 *C* equating to 1 h and so forth, and the discharging current was consistently fixed at 0.2 *C*. Capacities corresponding to 91.3%, 87.7%, 84.8%, and 77.5% (≈3.1 mAh cm^{-2} for the anode with a negative/positive ratio of ≈1.1) were achieved for the pouch cell employing the LPS/graphite electrode within timeframes of 30, 20, 15, and 10 min (corresponding to 2, 3, 4, and 6 *C*), respectively. Contrastingly, a mere 60.1% recharge was attained for the pouch cell equipped with a regular graphite electrode at 6 *C*. Furthermore, the cell exhibited a precipitous decline in capacity during the cycling process. Figure 4b,c and Figure S18 (Supporting Information) showed the charging/discharging profiles of pouch cells with two different graphite electrodes at various charging rates and the corresponding capacity contributions at the CC and CV charging states, respectively. The cells with LPS/graphite electrodes demonstrated a much higher percentage of the capacity in the CC state, in comparison with those with regular graphite electrodes. Specifically, at the CC charging rate of 6 *C*, the cell with the LPS/graphite electrode achieved a substantial capacity contribution of 65% at the CC state, which is markedly higher than the 16% observed for the cell with the regular graphite electrode (Figure 4c). This result substantiates the superior ionic transport capability of the LPS/graphite electrode compared to the regular graphite electrode. In comparison to cells based on the LPS/graphite electrode, those employing the regular graphite electrode rapidly reached the cut-off voltage, demonstrating substantial polarization under the fast-charging conditions (Figure S18, Supporting Information). This phenomenon is considered the principal factor contributing to the formation of metallic Li plating on the anode surface.[17] Table S1 (Supporting Information) and Figure 4d present a comparison

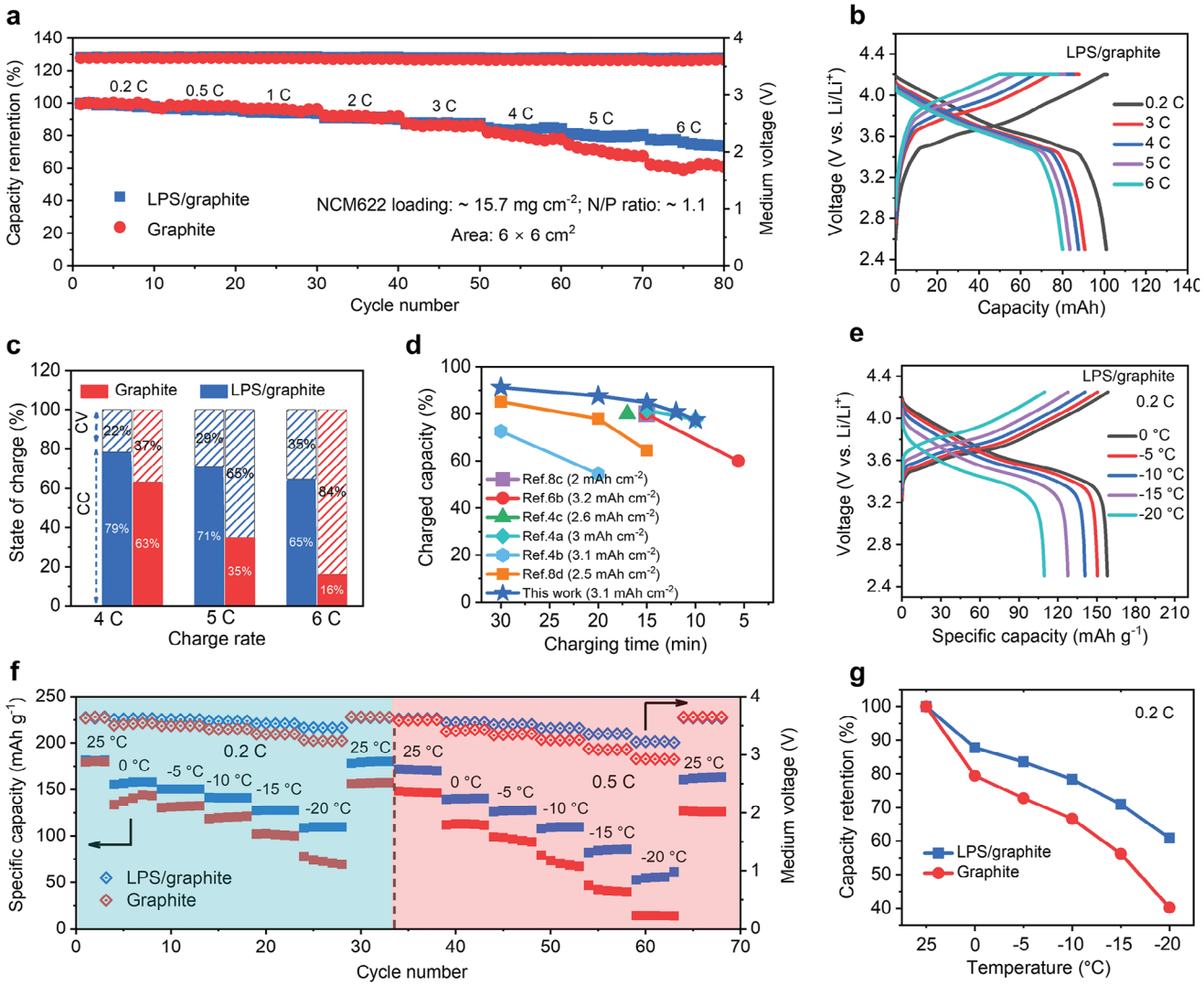

Figure 4. a) The fast-charging capability of different NCM622||graphite pouch cells with charging current range from 0.2 to 6 *C* and fixed discharging current of 0.2 *C*. b) Charging/discharging profiles of the LPS/graphite electrode at various charging current densities. c) Plots of the state of charge divided into CC/CV stages at different charging current densities. d) Comparison of the fast-charging capability of the LPS/graphite electrode with the reported graphite electrodes. e) Charging/discharging profiles of the LPS/graphite electrode at different test temperatures with a constant current of 0.2 *C*. f,g) Specific capacities of the two different NCM622||graphite cells at different temperature ranges from 25 to −20°C (f) and the corresponding capacity retentions (g).

of the fast-charging capability of cells using LPS/graphite electrodes with those reported in the literature, further underscoring the advancement of solid/liquid dual-phase Li^+ transport within the electrodes. Beyond their exceptional fast-charging capability, NCM622||LPS/graphite full cells also exhibited commendable performance at low temperatures. The charging/discharging profiles of the full cells, equipped with two graphite electrodes and tested at different temperatures, were shown in Figure 4e and Figure S19 (Supporting Information), respectively. It is revealed that an increase in polarization was observed in both types of full cells as the test temperature was reduced, attributable to the deceleration of reaction kinetics at lower temperatures. Nevertheless, the polarization voltages of the NCM622||LPS/graphite cell were significantly lower than that of the NCM622||graphite cell, suggesting an enhancement in the low-temperature performance of the LPS/graphite electrode. Figure 4f,g compares the electrochemical performance of NCM622||LPS/graphite and NCM622||graphite cells at different temperatures. Although the two cells have similar specific capacities (≈180.0 mAh g^{-1}, 0.2 *C*) at 25 °C, the NCM622||LPS/graphite cell delivered higher capacities at low temperatures. For the NCM622||LPS/graphite cell, specific capacities of 158.1 mAh g^{-1} (87.8%), 140.9 mAh g^{-1} (78.3%), and 109.6 mAh g^{-1} (60.9%) were achieved at 0, −10, and −20 °C, respectively. These values are significantly higher than those of the NCM622||graphite cell, which only realized capacities of 137.3 mAh g^{-1} (76.2%), 118.4 mAh g^{-1} (65.7%), and 70.8 mAh g^{-1} (39.3%) at the corresponding temperatures. The improved low-temperature performance of LPS/graphite electrode was attributed to its superior ionic transport capability compared to the regular graphite electrode. Contrary to the NCM622||graphite

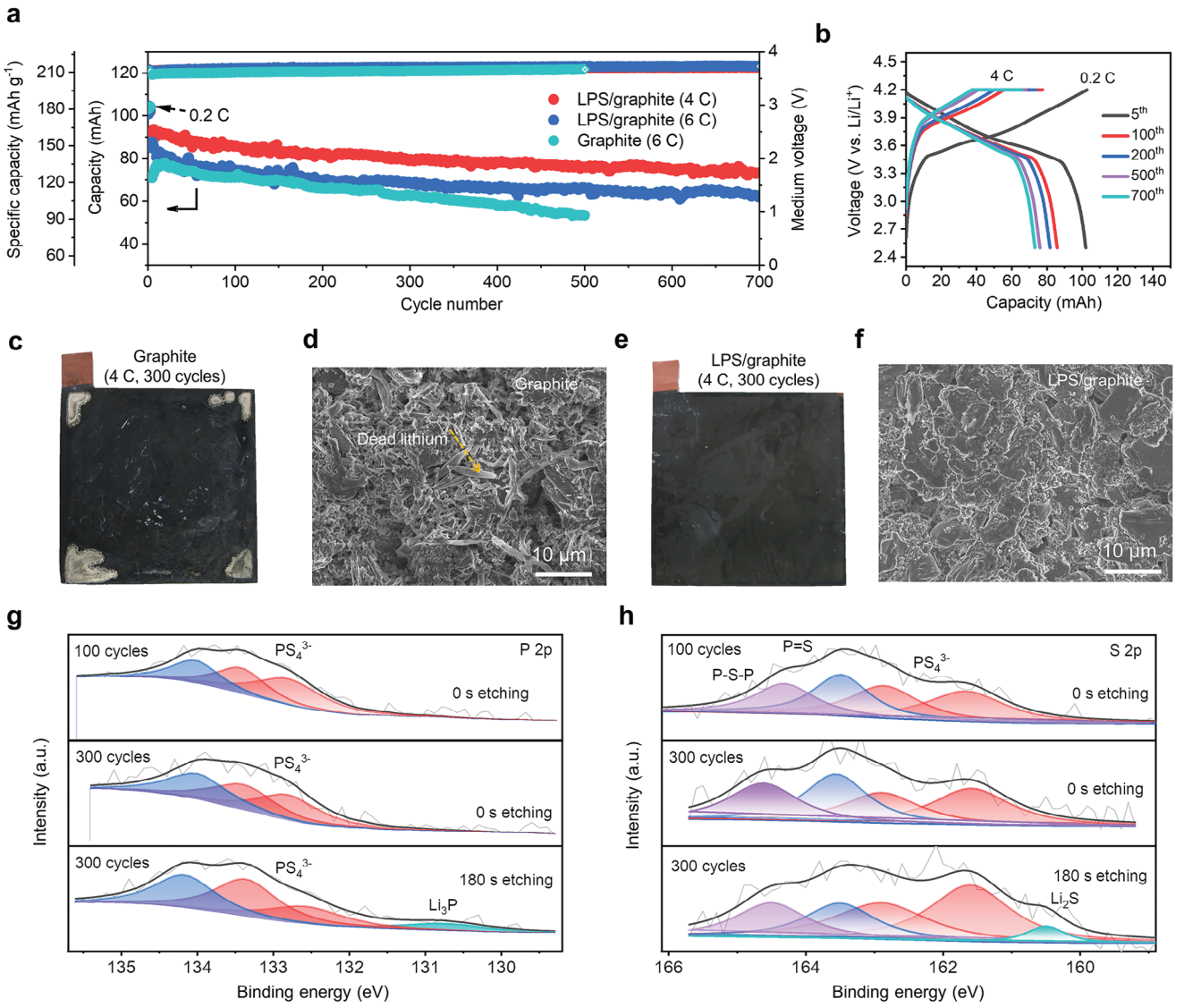

Figure 5. a,b) Cycling performance of the two different NCM622||graphite pouch cells at charging current at 4 *C* and 6 *C* (a) and the corresponding charging/discharging profiles (b). c–f) Digital and SEM images of the regular graphite (c,d) and LPS/graphite (e,f) electrodes after 300 cycles with a charging current of 4 *C*. g,h) High-resolution XPS P 2p (g) and S 2p (h) spectra of the LPS/graphite electrodes after different cycles.

cell, the NCM622||LPS/graphite cell is capable of fully restoring its original capacity at 25 °C, even following an operation at a low temperature of −20 °C (Figure 4f). This further substantiates the assertion that the solid/liquid dual-phase Li^+ transport within the electrode effectively suppresses Li plating behavior.

Achieving a long cycle lifespan under fast-charging conditions is of paramount importance. As shown in **Figure 5a**, the NCM622||LPS/graphite pouch cell showed high specific capacities of 160.1 and 148.3 mAh g^{-1} at 4 and 6 *C*, respectively. Furthermore, it demonstrates high capacity retentions of 80% (equivalent to 128.1 mAh g^{-1}) and 74% (equivalent to 109.4 mAh g^{-1}) after 700 cycles at 4 and 6 *C*, respectively. Moreover, it exhibits only a marginal increase in overpotential following extensive cycling (Figure 5b; Figure S20a, Supporting Information). Consequently, the achievement of the fast-charging capability of the cells with the LPS/graphite electrodes does not compromise their cycling performance. In contrast, the cell with the regular graphite electrodes showed a low initial specific capacity (135.9 mAh g^{-1}), with a capacity retention of 68% (93.3 mAh g^{-1}) following 500 cycles at 6 *C* (Figure 5a). This cell also demonstrated a substantial increase in overpotential during the cycling process (Figure S20b, Supporting Information). The polarization after 500 cycles was notably more severe in comparison to the NCM622||LPS/graphite cell (Figure S20c, Supporting Information). The morphology and structure of the graphite electrodes were investigated following 300 fast charging cycles at 4 *C*. As revealed by the optical photographs and SEM images depicted in Figure 5c–f, a portion of the regular graphite electrode was observed to be coated with silvery grey deposits (Figure 5c), and an abundance of dendritic metallic lithium was discernible under SEM (Figure 5d; Figure S21a, Supporting Information). The undesirable phenomenon of lithium plating on the graphite electrode surface not only

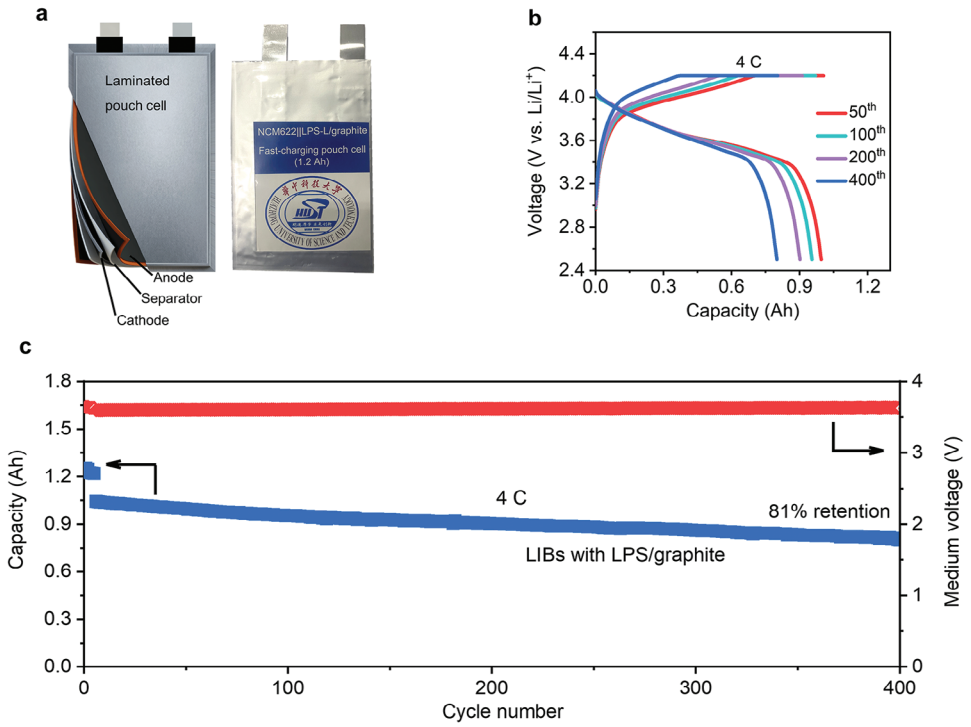

Figure 6. a) Schematic of laminated pouch cell and the photographs. b) Charging/discharging profiles of the laminated NCM622||LPS/graphite pouch cell at different cycles. c) Cycling performance of the laminated NCM622||LPS/graphite pouch cell (≈1.2 Ah at 0.2 *C*).

results in irreversible consumption of active lithium, thereby explaining the capacity degradation observed in pouch cells with regular graphite electrodes, but also raises significant safety concerns. In contrast, the cycled LPS/graphite electrode exhibited a smooth, clean surface, devoid of any observable metallic lithium deposits on its surface (Figure 5e,f; Figure S21b, Supporting Information). This observation aligns well with the remarkable fast-charging performance with long cycle lifespan demonstrated by this electrode. The chemical state of LPS/graphite after 100 cycles was analyzed by XPS. The high-resolution P 2p and S 2p XPS spectra of the LPS/graphite electrode after 100 cycles showed several split peaks (Figure 5g,h), which were similar to that of the initial LPS/graphite electrode. The characteristic peaks at 132.9 and 133.5 eV in the P 2p XPS spectrum can be ascribed to the PS_4^{3-} in the cycled electrodes[13,15] (Figure 5g). Meanwhile, the PS_4^{3-} signals were discernible in the S 2p XPS spectrum, positioned at 161.6 and 162.8 eV[16] (Figure 5h). Therefore, it can be concluded that LPS remained present in the electrode after multiple fast-charging cycles, which ensured the maintenance of swift Li^+ transport kinetics within the graphite electrode. The chemical state of the LPS/graphite electrode after 300 cycles was further scrutinized using XPS in conjunction with an Ar^+ sputtering depth profiling. The presence of PS_4^{3-} species was also detected on the electrode surface. The emergence of a new split peak, observed at 130.8 eV in the high-resolution P 2p spectrum and 160.5 eV in the high-resolution S 2p spectrum, corresponds to Li_3P and Li_2S,[18] respectively, which originated from the side reactions between LPS and graphite during the cycling.

To more comprehensively evaluate the potential of the LPS/graphite electrode in fast-charging LIBs, we constructed Ampere-hour (Ah) level laminated pouch cells coupling NCM622 as the cathode (**Figure** 6a). The NCM622||LPS/graphite pouch cell delivered a capacity of 1.20 Ah at 0.2 *C*. Remarkably, it sustained a capacity of 1.05 Ah at 4 *C*, suggesting that 87.5% of its total capacity can be recharged within 15 minutes (Figure 6b). According to the charging/discharging profiles, only slight potential polarization was observed during the cycling process(Figure 6c). This cell demonstrated robust cycling performance under fast charging conditions, preserving 81% of its capacity after 400 cycles at 4 *C* (Figure 6d). The exceptional fast-charging performance coupled with cycling stability highlights the potential of solid/liquid dual-phase Li^+ transport within the electrode in enhancing the reaction kinetics and extending the cycle life of graphite electrodes. The energy density of the cell was evaluated according to the detailed parameters of the cell listed in Table S2 (Supporting Information). Upon charging for 15 min, the energy density of this cell reached ≈221.5 Wh kg^{-1}, further demonstrating the practical applicability of the LPS/graphite electrode for extremely fast-charging batteries.

3. Conclusion

In summary, ionically conductive 3D LPS networks were effectively incorporated into graphite electrodes via an in situ conversion strategy involving P_4S_{16}. Owing to the single ionic conductor properties of LPS, the concentration polarization in the electrode during battery fast charging, as well as the interfacial resistance of graphite, were significantly mitigated. In conjunction with the regular liquid-phase electrolyte Li^+ transport, the as-resultant solid/liquid dual-phase Li^+ transport mechanism

facilitated accelerated electrochemical reaction kinetics within the LPS/graphite electrode. Consequently, the full cells with practical anode capacity exceeding 3 mAh cm^{-2} demonstrated superior fast charging performance, extended cycle lifespan, and commendable low-temperature performance. Notably, an Ah-level NCM622||LPS/graphite pouch cell exhibited stable cycling under the fast charging condition (4 *C*) and delivered a high energy density of ≈221.5 Wh kg^{-1} within a charging duration of 15 minutes. Such a graphite electrode design effectively addresses the significant trade-off between the fast-charging performance and high energy density inherent in LIBs and offers a promising avenue for the realization of the fast-charging LIBs with high energy density.

Supporting Information

Supporting Information is available from the Wiley Online Library or from the author.

Acknowledgements

S.T. and Y.Z. contributed equally to this work. This work is financially supported by the Natural Science Foundation of China (Grant No. 52072137). The authors would like to thank the Analytical and Testing Center of Huazhong University of Science and Technology (HUST) for providing the facilities to conduct the characterizations.

Conflict of Interest

The authors declare no conflict of interest.

Data Availability Statement

The data that support the findings of this study are available from the corresponding author upon reasonable request.

Keywords

fast charging, graphite electrode, high areal capacity, high energy density, hybrid solid/liquid electrolyte

Received: February 2, 2024
Revised: March 1, 2024
Published online:

[1] a) W. Cai, Y.-X. Yao, G.-L. Zhu, C. Yan, L.-L. Jiang, C. He, J.-Q. Huang, Q. Zhang, *Chem. Soc. Rev.* **2020**, *49*, 3806; b) Y. Liu, Y. Zhu, Y. Cui, *Nat. Energy* **2019**, *4*, 540; c) C.-Y. Wang, T. Liu, X.-G. Yang, S. Ge, N. V. Stanley, E. S. Rountree, Y. Leng, B. D. McCarthy, *Nature* **2022**, *611*, 485; d) S. Tu, Z. Lu, M. Zheng, Z. Chen, X. Wang, Z. Cai, C. Chen, L. Wang, C. Li, Z. W. Seh, S. Zhang, J. Lu, Y. Sun, *Adv. Mater.* **2022**, *34*, 2202892; e) Y. Ma, S. Li, Y. An, Q. Peng, X. Zhang, X. Sun, K. Wang, Y. Ma, *Energy Storage Mater.* **2023**, *62*, 102946; f) Z. Zhao, X. Zhao, Y. Zhou, S. Liu, G. Fang, S. Liang, *Adv. Powder Mater.* **2023**, *2*, 100139.

[2] a) Q. Ni, L. Zheng, Y. Bai, T. Liu, H. Ren, H. Xu, C. Wu, J. Lu, *ACS Energy Lett.* **2020**, *5*, 1763; b) S. Li, K. Wang, G. Zhang, S. Li, Y. Xu, X. Zhang, X. Zhang, S. Zheng, X. Sun, Y. Ma, *Adv. Funct. Mater.* **2022**, *32*, 2200796.

[3] a) S. Ahmed, I. Bloom, A. N. Jansen, T. Tanim, E. J. Dufek, A. Pesaran, A. Burnham, R. B. Carlson, F. Dias, K. Hardy, M. Keyser, C. Kreuzer, A. Markel, A. Meintz, C. Michelbacher, M. Mohanpurkar, P. A. Nelson, D. C. Robertson, D. Scoffield, M. Shirk, T. Stephens, R. Vijayagopal, J. Zhang, *J. Power Sources* **2017**, *367*, 250; b) C. Mao, R. E. Ruther, J. Li, Z. Du, I. Belharouak, *Electrochem. Commun.* **2018**, *97*, 37.

[4] a) K. H. Chen, V. Goel, M. J. Namkoong, M. Wied, S. Müller, V. Wood, J. Sakamoto, K. Thornton, N. P. Dasgupta, *Adv. Energy Mater.* **2020**, *11*, 2003336; b) L. L. Lu, Z. X. Zhu, T. Ma, T. Tian, H. X. Ju, X. X. Wang, J. L. Peng, H. B. Yao, S. H. Yu, *Adv. Mater.* **2022**, *34*, 2202688; c) M. Baek, J. Kim, J. Jin, J. W. Choi, *Nat. Commu.* **2021**, *12*, 6807.

[5] a) Q. Cheng, Y. Zhang, *J. Electrochem. Soc.* **2018**, *165*, A1104; b) S. S. Zhang, L. Ma, J. L. Allen, J. A. Read, *J. Electrochem. Soc.* **2021**, *168*, 2202688; c) S.-M. Lee, J. Kim, J. Moon, K.-N. Jung, J. H. Kim, G.-J. Park, J.-H. Choi, D. Y. Rhee, J.-S. Kim, J.-W. Lee, M.-S. Park, *Nat. Commun.* **2021**, *12*, 39; d) S. Tu, B. Zhang, Y. Zhang, Z. Chen, X. Wang, R. Zhan, Y. Ou, W. Wang, X. Liu, X. Duan, L. Wang, Y. Sun, *Nat. Energy* **2023**, *8*, 1365.

[6] a) J. Billaud, F. Bouville, T. Magrini, C. Villevieille, A. R. Studart, *Nat. Energy* **2016**, *1*, 16097; b) L.-L. Lu, Y.-Y. Lu, Z.-X. Zhu, J.-X. Shao, H.-B. Yao, S. Wang, T.-W. Zhang, Y. Ni, X.-X. Wang, S.-H. Yu, *Sci. Adv.* **2022**, *8*, eabm6624.

[7] J. B. Habedank, J. Kriegler, M. F. Zaeh, *J. Electrochem. Soc.* **2019**, *166*, A3940.

[8] a) H. Gao, Q. Yan, J. Holoubek, Y. Yin, W. Bao, H. Liu, A. Baskin, M. Li, G. Cai, W. Li, D. Tran, P. Liu, J. Luo, Y. S. Meng, Z. Chen, *Adv. Energy Mater.* **2022**, *13*, 2202906; b) L. L. Jiang, C. Yan, Y. X. Yao, W. Cai, J. Q. Huang, Q. Zhang, *Angew. Chem., Int. Ed.* **2020**, *60*, 3402; c) C. Sun, X. Ji, S. Weng, R. Li, X. Huang, C. Zhu, X. Xiao, T. Deng, L. Fan, L. Chen, X. Wang, C. Wang, X. Fan, *Adv. Mater.* **2022**, *34*, 2206020; d) J. Xu, J. Zhang, T. P. Pollard, Q. Li, S. Tan, S. Hou, H. Wan, F. Chen, H. He, E. Hu, K. Xu, X.-Q. Yang, O. Borodin, C. Wang, *Nature* **2023**, *614*, 694; e) H. Zhang, Z. Song, J. Fang, K. Li, M. Zhang, Z. Li, L. Yang, F. Pan, *J. Phy. Chem. C* **2023**, *127*, 2755.

[9] M. Doyle, T. F. Fuller, J. Newman, *Electrochim. Acta* **1994**, *39*, 2073.

[10] K. M. Diederichsen, E. J. McShane, B. D. McCloskey, *ACS Energy Lett.* **2017**, *2*, 2563.

[11] J. Lau, R. H. DeBlock, D. M. Butts, D. S. Ashby, C. S. Choi, B. S. Dunn, *Adv. Energy Mater.* **2018**, *8*, 1800933.

[12] D. Wei, J. Yin, Z. Ju, S. Zeng, H. Li, W. Zhao, Y. Wei, H. Li, *J. Energy Chem.* **2020**, *50*, 187.

[13] J. Liang, X. Li, Y. Zhao, L. V. Goncharova, G. Wang, K. R. Adair, C. Wang, R. Li, Y. Zhu, Y. Qian, L. Zhang, R. Yang, S. Lu, X. Sun, *Adv. Mater.* **2018**, *30*, 1804684.

[14] a) X. Li, J. Liang, M. N. Banis, J. Luo, C. Wang, W. Li, X. Li, Q. Sun, Y. Hu, Q. Xiao, T.-K. Sham, L. Zhang, S. Zhao, S. Lu, H. Huang, R. Li, X. Sun, *Energy Storage Mater.* **2020**, *28*, 325; b) X. Li, J. Liang, Y. Lu, Z. Hou, Q. Cheng, Y. Zhu, Y. Qian, *Angew. Chem., Int. Ed.* **2017**, *56*, 2937.

[15] Q. Pang, X. Liang, A. Shyamsunder, L. F. Nazar, *Joule* **2017**, *1*, 871.

[16] M. R. Busche, D. A. Weber, Y. Schneider, C. Dietrich, S. Wenzel, T. Leichtweiss, D. Schröder, W. Zhang, H. Weigand, D. Walter, S. J. Sedlmaier, D. Houtarde, L. F. Nazar, J. Janek, *Chem. Mater.* **2016**, *28*, 6152.

[17] N. Kim, S. Chae, J. Ma, M. Ko, J. Cho, *Nat. Commun.* **2017**, *8*, 812.

[18] D. H. S. Tan, E. A. Wu, H. Nguyen, Z. Chen, M. A. T. Marple, J.-M. Doux, X. Wang, H. Yang, A. Banerjee, Y. S. Meng, *ACS Energy Lett.* **2019**, *4*, 2418.